

Probing Entanglement Scaling Across a Quantum Phase Transition on a Quantum Computer

Qiang Miao,¹ Tianyi Wang,² Kenneth R. Brown,^{1, 3, 2, 4} Thomas Barthel,^{2, 1, *} and Marko Cetina^{1, 2, 3, †}

¹*Duke Quantum Center, Duke University, Durham, North Carolina 27701, USA*

²*Department of Physics, Duke University, Durham, North Carolina 27708, USA*

³*Department of Electrical and Computer Engineering,*

Duke University, Durham, North Carolina 27708, USA

⁴*Department of Chemistry, Duke University, Durham, North Carolina 27708, USA*

(Dated: January 2025)

The investigation of strongly-correlated quantum matter is difficult due to the curse of dimensionality and intricate entanglement structures. These challenges are particularly pronounced in the vicinity of continuous quantum phase transitions, where quantum fluctuations manifest across all length scales. While quantum simulators give controlled access to a number of strongly correlated systems, the study of critical phenomena has been hampered by finite-size effects arising from diverging correlation lengths. Moreover, the experimental investigation of entanglement in many-body systems has been hindered by limitations in measurement protocols. To address these challenges, we employ the multiscale entanglement renormalization ansatz (MERA) and implement a holographic scheme for subsystem tomography on a fully-connected trapped-ion quantum computer. Our method accurately represents infinite systems and long-range correlations with few qubits, facilitating the efficient extraction of observables and entanglement properties, even at criticality. We observe a quantum phase transition with spontaneous symmetry breaking and reveal the evolution of entanglement properties across the critical point. For the first time, we demonstrate log-law scaling of subsystem entanglement entropies at criticality on a digital quantum computer. This achievement highlights the potential of MERA for the investigation of strongly-correlated many-body systems on quantum computers.

I. INTRODUCTION

In physics and materials science, *universality* appears near continuous phase transitions, where long-range properties become independent of microscopic details, and physical quantities like correlation lengths are characterized by universal critical exponents. While classical phase transitions are driven by thermal fluctuations, quantum phase transitions occur at zero temperature when a system parameter is varied, causing the ground state to become highly entangled due to quantum fluctuations [1, 2]. This groundstate non-locality presents challenges for theoretical and experimental analysis.

Rapid advancements on controlled quantum platforms have expanded the range of experimentally accessible quantum many-body systems on quantum simulators and computers [3–10]. Previous studies [11–18] have made significant progress in the experimental characterization of entanglement. However, probing entanglement properties across quantum phase transitions remains difficult. Analog quantum simulators have limited control, restricting available models and measurements [19]. Quantum simulations using quantum computers face challenges including: (i) *Limited number of qubits*: Quantum phase transitions formally occur only in infinite systems, and finite-size effects are pronounced near critical points. Preparing critical ground states requires more

qubits than current quantum devices offer. (ii) *Exponential cost for probing subsystem entanglement*: Resolving detailed entanglement structures requires state tomography for large subsystems, which generally results in exponential costs. (iii) *Difficulties in state preparation*: Without deeper insight into the physics, the study of complex many-body ground states necessitates highly expressive quantum circuits with many gates, leading to low trainability [20, 21] and significant error accumulation.

We overcome these challenges for condensed-matter ground states using highly structured quantum circuits on a digital quantum computer. The circuits prepare states corresponding to hierarchical tensor networks—the multiscale entanglement renormalization ansatz (MERA) [22–24]. This ansatz can represent infinite systems and accurately encodes long-range correlations, even at critical points. The causal structure of MERA, inspired by the real-space renormalization group, drastically reduces circuit depths and the number of measured qubits, both scaling logarithmically with system size [25–28]. This allows efficient extraction of local observables, subsystem entanglement, and entanglement spectra. Additionally, MERA is robust to noise [29] and not affected by barren plateaus [30, 31].

In this work, we study quantum many-body ground states on a digital quantum computer based on a chain of ytterbium ions. We demonstrate a quantum phase transition characterized by spontaneous symmetry breaking in the thermodynamic limit, using 12 or fewer qubits. We show the universal scaling of relevant physical quantities near the transition and observe significant changes in the

* thomas.barthel@duke.edu

† marko.cetina@duke.edu

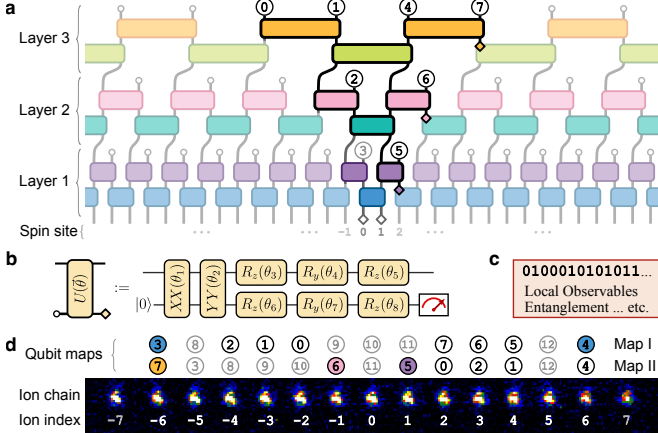


FIG. 1. MERA on a trapped-ion chain. (a) An infinite, binary 1D MERA with three homogeneous layers. The ansatz is prepared from top to bottom, with each layer comprising entangling gates and isometries that double the number of sites. The output is the many-body state on the physical spin sites. Repeating the MERA circuit horizontally in the spatial dimension generates a state in the thermodynamic limit. Local observables and bipartite entanglement can be studied by executing circuits within the corresponding causal cone (unshaded area) and measuring the target qubits. (b) Each MERA tensor is implemented as a sequence of two- and one-qubit gates. Open circles represent qubits initialized in $|0\rangle$, and diamonds indicate measurements. (c) Repeated preparation and measurement yield probabilistic binary outcomes (0s and 1s) from which the desired physical properties can be inferred. (d) Fluorescence image of a 15-ion ($^{171}\text{Yb}^+$) chain with two hardware-tailored examples of ion-to-qubit mappings: Map I for local measurements on sites 0 and 1, and Map II optimized for entanglement studies with respect to a bipartition into the semi-infinite subsystems $A = (-\infty, 1]$ and $B = [2, \infty)$.

entanglement structure across the critical point. At the critical point, we find that the subsystem entanglement entropies follow a universal log-area law, and the gap of the entanglement Hamiltonian closes as the subsystem size increases. In non-critical regimes, subsystem entanglement entropy follows an area law [32–34]. The measured entanglement Hamiltonian remains gapped with increasing subsystem size and accurately reproduces expected symmetry properties.

II. MERA AND HOLOGRAPHIC SUBSYSTEM TOMOGRAPHY

To approximate the ground state $|\Psi\rangle$ in the thermodynamic limit, we implement MERA on a digital ion-trap quantum computer. We confine fifteen $^{171}\text{Yb}^+$ ions in a micro-fabricated Paul trap and address them individually with laser beams (see Appendix A). The all-to-all qubit connectivity of our platform simplifies the implementation of the non-local MERA circuits. Using a detailed error model discussed in Appendix E, we optimize ion-

to-qubit mappings for each MERA circuit; see Fig. 1(d).

As shown in Fig. 1(a), the layered MERA structure introduces an additional dimension associated with a hierarchy of length and energy scales. MERA comprises T layers of isometries and unitary entanglers. Preparing the MERA from top to bottom, one first generates longer-range correlations (lower energy scales) and progressively incorporates shorter-range correlations (higher energy scales). Viewed in reverse, MERA acts as a renormalization group flow, systematically removing short-distance entanglement by disentanglers and then coarse-graining by projections (open circles) at each renormalization step until the final layer $T \sim \log \xi$ is reached, where ξ is the largest correlation length in the system.

Local observables can be studied by preparing only the corresponding causal-cone circuits. For measurements on sites 0 and 1 of a binary one-dimensional (1D) MERA, the reduced circuit is indicated by the non-shaded MERA tensors in Fig. 1(a). The shaded tensors outside the causal cone do not influence the local measurements.

Entanglement entropies and spectra for a spatial bipartition into parts A and B can be obtained from the reduced density matrix $\hat{\rho}_B = \text{Tr}_A |\Psi\rangle\langle\Psi|$. For a MERA, only the gates within the causal cone of the *boundary* between A and B need to be implemented, as gates outside the causal cone correspond to unitary basis transformations \hat{U}_A and \hat{U}_B in the two subsystems and do not affect bipartite entanglement properties. Moreover, tomography on the renormalized sites (qubits) at the edges of A 's causal cone provides access to $\hat{\rho}_B$ in the basis defined by \hat{U}_B . Thus, due to the causal structure of MERA, the number of gates and number of measured qubits are proportional to the number of layers $T \sim \log \xi$, rather than the total system size and subsystem size, respectively. Details of our scheme, termed *holographic subsystem tomography*, are described in Appendix B.

In the experiment, we implement an infinite, homogeneous, binary 1D MERA with bond dimension $\chi = 2$ and up to $T = 5$ layers. This ansatz captures a maximum correlation range of $3 \times 2^5 = 96$ sites. For the self-similar critical systems, the correlation length ξ diverges, which we address by employing a scale-invariant MERA [35, 36] as discussed in Sec. III B 2 and Appendix D.

III. RESULTS

To benchmark the MERA approach, we apply it to the 1D transverse-field Ising model (TFIM) described by the Hamiltonian

$$\hat{H} = - \sum_i^L \hat{X}_i \hat{X}_{i+1} - g \sum_i^L \hat{Z}_i. \quad (1)$$

Here, \hat{X}_i and \hat{Z}_i are Pauli operators acting on the spin at lattice site i , and g is the transverse magnetic field. The TFIM features a well-characterized continuous quan-

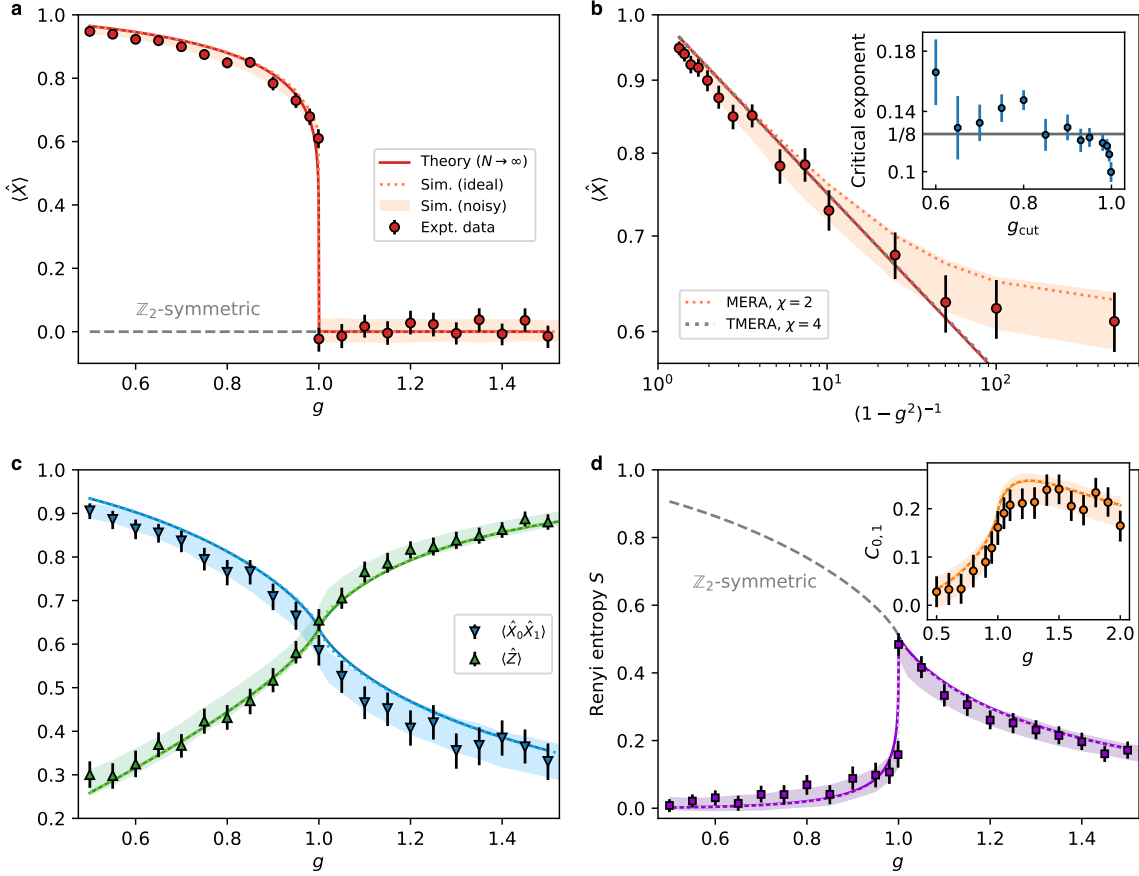


FIG. 2. Local observables and few-site entanglement in the 1D transverse-field Ising model as function of the field g . (a) Mean magnetization $\langle \hat{X} \rangle$. The dashed gray line represents the reference value for a \mathbb{Z}_2 -symmetric state. (b) Logarithmic plot of $\langle \hat{X} \rangle$ in the \mathbb{Z}_2 symmetry-broken ferromagnetic phase ($g < 1$). The orange and gray dotted lines show the theoretical predictions for MERA with bond dimension $\chi = 2$ and Trotterized MERA [26, 27] with $\chi = 4$, respectively. The inset displays the critical exponent obtained from fitting the data on intervals $g \in [0.5, g_{\text{cut}}]$. Error bars indicate 1σ fitting uncertainties, and the theoretical critical exponent for the Ising class is $1/8$. (c) Local observables corresponding to the two competing terms in the Hamiltonian (1). (d) The Rényi-2 entanglement entropy of a single spin. The dashed gray line corresponds to the \mathbb{Z}_2 -symmetric ground state. The inset shows the nearest-neighbor concurrence $C_{0,1}$ (pairwise entanglement) for two neighboring sites. For all panels, solid lines correspond to theoretical predictions in the thermodynamic limit, dotted lines represent ideal infinite MERA simulations, and the shaded areas indicate the central 95% quantile obtained from noisy simulations based on an error model that reflects experimental device characteristics. Unless otherwise noted, error bars indicate 95% confidence intervals obtained from a bootstrap resampling of the experimental data, based on 2,000 measurements per quantum circuit.

tum phase transition with spontaneous \mathbb{Z}_2 symmetry-breaking, making it a good testbed for our approach.

A. Quantum phase transition

We benchmark the infinite MERA for the ground state of the TFIM (1) by measuring the local observables $\langle \hat{O}_i \rangle$. We prepare the causal-cone state of the target spins as indicated in Fig. 1. The number T of employed MERA layers ranges from 2 to 5, depending on the correlation length; $T = 2$ layers are used far from criticality and up to 5 layers near the critical point $g = 1$. Correspondingly,

the number of required qubits ranges from 6 to 12.

Figure 2(a) shows the measured magnetization $\langle \hat{X} \rangle$ in the x -direction as a function of the z -field g , nicely resolving the phase transition. For $g > 1$, the observed magnetization is consistent with zero within the statistical uncertainty, as expected for the paramagnetic phase. For $g < 1$, non-zero magnetization is observed along the x -direction, indicating spontaneous breaking of the $\hat{X} \rightarrow -\hat{X}$ symmetry, characteristic of the ferromagnetic phase. Due to experimental noise, the observed magnetization at small g is slightly lower than the theoretical prediction $\langle \hat{X} \rangle = (1-g^2)^{1/8}$ in the thermodynamic limit $L \rightarrow \infty$ [37–39].

We conducted separate experiments to characterize noise and develop a corresponding error model, as described in Appendix E. In simulations, we model gate-induced dephasing and addressing noise due to ion motion by randomly perturbing gates in each shot. We model idle dephasing, state preparation and measurement (SPAM) errors, and X -flip errors during entangling gates by introducing random Z - and X -flips. The noisy simulations (shaded area in Fig. 2(a)) demonstrate excellent agreement with experimental data.

To determine the critical exponent, Fig. 2(b) displays the order parameter $\langle \hat{X} \rangle$ on a logarithmic scale. Due to the small MERA bond dimension $\chi = 2$, $\langle \hat{X} \rangle$ saturates at a non-zero value as the system approaches the critical regime. Nevertheless, it is still possible to determine the critical scaling from these experimental data. The inset shows the critical exponent obtained by fitting the data in ranges $g \in [0.5, g_{\text{cut}}]$. The fitted values gradually converge to the theoretical prediction of $1/8$ but deviate when g_{cut} approaches $g = 1$. Such deviations near the critical point can be mitigated by increasing the bond dimension χ . As shown by the thick gray dotted line, a Trotterized MERA circuit [25–28] with $\chi = 4$ is predicted to achieve sufficient accuracy to eliminate the discrepancies at the cost of more qubits and gates.

Figure 2(c) shows additional local observables. As the transverse field g increases, the dominant contribution to the groundstate energy shifts from the correlator $\langle \hat{X}_i \hat{X}_{i+1} \rangle$ to the field term $\langle \hat{Z}_i \rangle$, showing a symmetry due to the Kramers-Wannier duality [40] with respect to the critical point $g = 1$. The measured values of these observables cross at a slightly smaller value of g , aligning with our noise model. Here, the noise is dominated by fluctuations in XX -gate rotations due to the ions' axial motion (see Appendix E3).

B. Entanglement structure

In the following, we use MERA to investigate ground-state entanglement across the quantum phase transition in the TFIM (1). We find that MERA on the digital quantum computer can resolve details of the entanglement structure, including the hallmark transition from area-law to log-area-law scaling of block entanglement entropies when approaching the critical point.

1. Local entanglement measures

For a pure state $|\Psi\rangle$, the entanglement between subsystem B and its complement A can be quantified by the Rényi entanglement entropy

$$S_B^{(\alpha)} = \frac{1}{1 - \alpha} \log_2 \text{Tr}(\hat{\rho}_B^\alpha), \text{ where } \hat{\rho}_B = \text{Tr}_A |\Psi\rangle\langle\Psi| \quad (2)$$

is the reduced density matrix of subsystem B . Our approach provides efficient access to the entanglement spec-

tra and, hence, $S_B^{(\alpha)}$ for any α . Here, we focus on the Rényi-2 entropy ($\alpha = 2$) as, for the TFIM (1), all Rényi entropies with $\alpha > 0$ exhibit the same scaling.

The reduced density matrix for a single-site is fully characterized by its Bloch vector. The time-reversal symmetry of the TFIM ensures that the local expectation value $\langle \hat{Y} \rangle$ vanishes for all eigenstates. Thus, the Bloch vector is determined by $\langle \hat{X} \rangle$ and $\langle \hat{Z} \rangle$. Figure 2(d) shows the measured single-site Rényi-2 entanglement entropy. Our data faithfully reproduces the predicted sharp peak at criticality and tends to zero for small g . In the ferromagnetic phase, the two symmetry-broken ground states are almost product states. Meanwhile, their symmetric superposition is entangled, and the corresponding single-site entanglement is smooth at the critical point.

The inset of Fig. 2(d) presents the nearest-neighbor concurrence (pairwise entanglement) $C_{0,1}$ [39, 42] obtained from the measured nearest-neighbor correlators $\langle \hat{X}_0 \hat{X}_1 \rangle$, $\langle \hat{Z}_0 \hat{Z}_1 \rangle$, and $\langle \hat{Y}_0 \hat{Y}_1 \rangle$ [43, 44]. The concurrence slightly deviates from theoretical predictions but aligns well with noisy simulations. Notably, the concurrence does not peak at criticality but increases smoothly before reaching a broad maximum in the paramagnetic phase. This suggests that the peak of single-site entanglement at criticality arises not only from short-distance entanglement but also from the accumulation of entanglement over long distances. In contrast, in the paramagnetic phase, the nearest-neighbor entanglement is the dominant contribution to the single-site entanglement.

2. Entanglement scaling: area-law versus log-area-law

For the ground states of typical quantum many-body systems in D spatial dimensions, the subsystem entanglement entropy $S(\ell)$ is proportional to the surface area of the subsystem $\propto \ell^{D-1}$, rather than its volume $\propto \ell^D$ [32–34]. The entanglement entropy is dominated by short-range correlations around the subsystem boundary, resulting in area-law scaling. This can change when the system becomes critical and the correlation length diverges. For critical systems in 1D and fermionic systems with a Fermi surface of codimension $D-1$, the subsystem entanglement entropy is predicted to follow a log-area law $\propto \ell^{D-1} \log \ell$ [45–50].

Resolving these fundamentally different scaling laws has remained an experimental challenge. In small systems, it is difficult to differentiate between log-area-law and area-law scalings. As the linear subsystem size ℓ grows, preparing ground states with sufficient precision becomes increasingly difficult, and, in direct approaches, the number of measurements needed for subsystem tomography grows exponentially in ℓ .

For MERA, however, each step of the renormalization process changes length scales by a constant factor. This maps a logarithmic scaling in the subsystem size ℓ to a linear scaling in the number of renormalization steps $T = 1, 2, 3, \dots$. Thus, distinguishing between area and

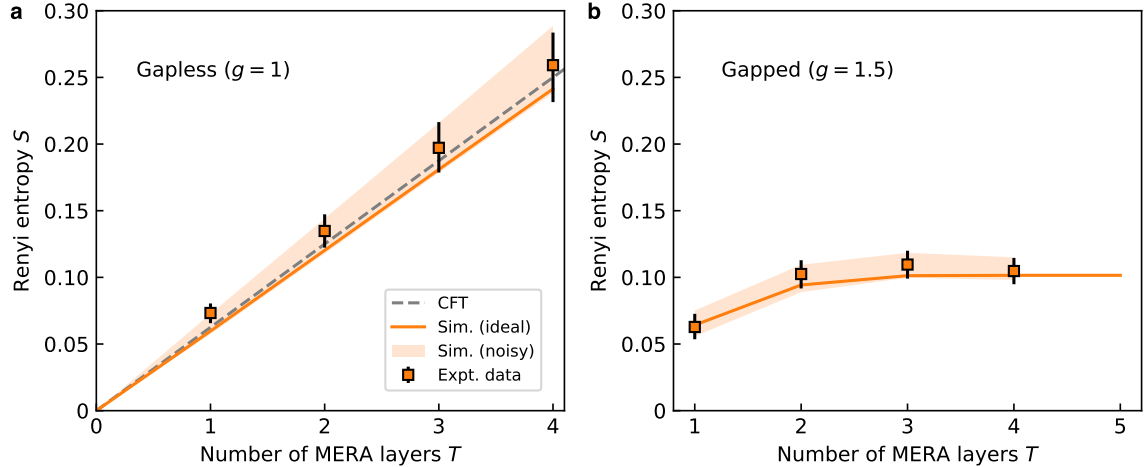


FIG. 3. **Log-area-law and area-law scaling of entanglement entropy for critical and gapped systems.** (a) Bipartite half-chain Rényi-2 entanglement entropy for the infinite Ising chain (1) at the critical point $g = 1$ depending on the number T of MERA layers. The effective subsystem size is $\ell = 3 \times 2^T$. The gray dashed line shows the log-area law prediction of conformal field theory (CFT) with central charge $c = 1/2$, and the solid line corresponds to ideal MERA simulations. Both the noisy simulation (shaded area) and experimental data (dots with error bars) are shown with 95% confidence intervals based on 1,500 shots per element of the tomographic measurement basis. (b) Rényi-2 entanglement entropy for MERA states at the non-critical point $g = 1.5$. Here, the half-chain entanglement saturates rapidly as the number T of MERA layers increases, indicating the area law. The shaded area and error bars show 95% confidence intervals based on 8,000, 5,000, 3,000, and 2,000 shots per measurement basis element for cases with one-, two-, three-, and four-layer MERA, respectively.

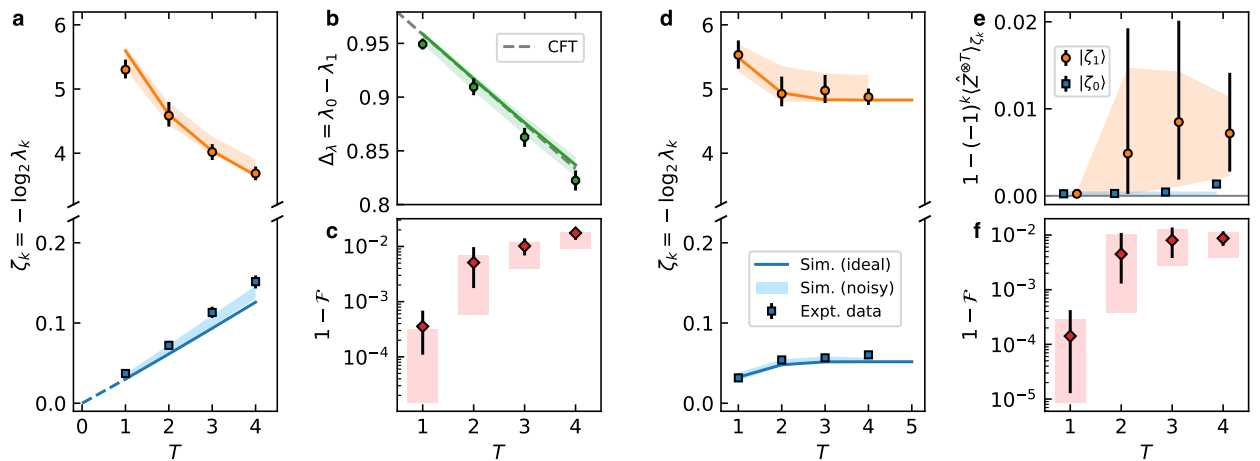


FIG. 4. **Analysis of half-chain density matrices.** (a) and (d) T -dependence of the lowest two eigenvalues $\{\zeta_0, \zeta_1\}$ of the MERA entanglement Hamiltonian at the critical point $g = 1$ and the non-critical point $g = 1.5$, respectively. (b) The Schmidt gap $\Delta_\lambda = \lambda_0 - \lambda_1$ gradually closes as the (sub)system size increases at criticality. The gray dashed line represents the theoretical approximation from Ref. [41]. (c) and (f) Infidelity of the subsystem density matrices relative to ideal simulations at $g = 1$ and $g = 1.5$, respectively. (e) Expectation values of Pauli Z -strings for the first two eigenstates $\{|\zeta_0\rangle, |\zeta_1\rangle\}$ of the entanglement Hamiltonian at $g = 1.5$. In all plots, solid lines represent ideal infinite MERA simulations. Both the noisy simulation (shaded area) and the experimental data (dots) are shown with indicators for the 95% confidence intervals. The results are based on the same dataset as Fig. 3, but here, positive semi-definite density matrices are reconstructed using maximum-likelihood estimation.

log-area laws in 1D translates to determining whether the entanglement entropy saturates or grows linearly with increasing T .

We experimentally realize spatially infinite MERA with a finite number of layers T . For a bipartition into subsystems $A = (-\infty, 1]$ and $B = [2, +\infty)$, we implement the holographic subsystem tomography as described in Sec. II and detailed in Appendix B. We prepare the MERA circuit within the causal cone of the subsystem boundary, measure the T renormalized sites at the right edge of the cone (Fig. 1), and use the classical shadow method [51] to extract the Rényi-2 entanglement entropy (2). The finite number of MERA layers limits the maximal correlation length to 3×2^T . Thus, we experimentally probe effective subsystem sizes $\ell \propto 2^T$. See Appendix C for a more detailed argument on this relation of T and effective subsystem sizes.

For the non-critical point $g = 1.5$ of the TFIM (1), the measured half-chain Rényi-2 entanglement entropy S is shown in Fig. 3(b). We observe a rapid saturation of the entanglement entropy for $T \geq 3$, in agreement with the area-law. This is expected as, due to the energy gap, the physical correlation length ξ is finite. Here, additional MERA layers ($T > 3$) have a negligible effect on the groundstate approximation and entanglement for this gapped system. Our error model indicates that, in this regime, SPAM errors and gate rotation errors due to ions' axial motion are the primary noise sources.

At criticality ($g = 1$), the system has gapless excitations, and the correlation length diverges ($\xi \rightarrow \infty$). Here, we model the ground state using a *scale-invariant* MERA with an infinite number of homogeneous identical layers in both the spatial and preparation directions [35, 36]. Directly preparing a scale-invariant MERA is not experimentally feasible. Instead, we truncate at layer T and add an additional tensor to the top layer to minimize the finite- T effects as detailed in Appendix D.

The measured half-chain Rényi-2 entanglement entropy S at criticality is shown as a function of T in Fig. 3(a). The observed entropy increases linearly by approximately 1/16 per MERA layer. This is consistent with the prediction $\frac{1}{16} \log_2(\ell/a)$ of conformal field theory, where a is an ultraviolet cutoff that regularizes the continuum field theory [52]. The slight increase in the measured S over the field-theoretical prediction is reproduced by our error model. Here, the primary error sources are SPAM errors, noise in gate angles due to ions' axial motion, X -flips, and idle dephasing (see Appendix E).

3. Entanglement spectrum

Using the holographic tomography data and a maximum-likelihood approach [53–56], we reconstruct proper (positive semidefinite) density matrices $\hat{\rho}_B$ for subsystem B in the \hat{U}_B basis. They can be written in the form $\hat{\rho}_B = 2^{-\sum_i \zeta_i |\zeta_i\rangle\langle\zeta_i|}$, where $\{\zeta_i := -\log_2 \lambda_i\}$ is the entanglement spectrum [57] expressed in terms of the

eigenvalues $\{\lambda_i\}$ of $\hat{\rho}_B$.

Figures 4(a) and (d) show the two lowest entanglement eigenvalues $\{\zeta_0, \zeta_1\}$ of $\hat{\rho}_B$ for the TFIM (1), revealing distinct behaviors at and away from the critical point. At criticality ($g = 1$), the lowest eigenvalue ζ_0 exhibits a log-law scaling like the entanglement entropy, while ζ_1 decreases with increasing T . As shown in Fig. 4(b), the Schmidt gap $\Delta_\lambda = \lambda_0 - \lambda_1$ reduces by approximately 1/24 per renormalization step, which agrees with the approximate theoretical prediction $\Delta_\lambda \sim \ell^{-1/24}$ from Ref. [41], where ℓ denotes again the (effective) subsystem size. For the non-critical point $g = 1.5$, Fig. 4(d) shows that ζ_0 and ζ_1 saturate with increasing T .

Since $g = 1.5$ lies in the \mathbb{Z}_2 -symmetric paramagnetic phase, all subsystem density matrices of the ground state must commute with the operator $\otimes_i \hat{Z}_i$. We verify this symmetry by measuring the spin-flip operator on subsystem B . As discussed in Sec. II, the measurement is done efficiently with the compressed representation of $\hat{\rho}_B$ on the renormalized sites, exploiting the fact that, for $g \geq 1$, the unitary \hat{U}_B which transforms the measured state to the actual state on B preserves the \mathbb{Z}_2 -symmetry. As observed in Fig. 4(e), the associated entanglement Hamiltonian exhibits a ground state in the even-parity sector and a first excited state in the odd sector. This mirrors the properties of the system Hamiltonian, aligning with recent efforts concerning connections between entanglement Hamiltonians and system Hamiltonians [17, 58].

4. Subsystem fidelity

Finally, we compare the reconstructed subsystem density matrix $\hat{\rho}_B$ in the \hat{U}_B basis with the ideal MERA simulations, and show the infidelity $1 - \mathcal{F}$ in Figs. 4c and f for the transverse fields $g = 1.0$ and 1.5 , where

$$\mathcal{F} = \left(\text{Tr} \sqrt{\sqrt{\hat{\rho}_B} \hat{\rho}_{\text{ideal}} \sqrt{\hat{\rho}_B}} \right)^2. \quad (3)$$

Owing to careful calibrations, optimized ion-qubit mappings, suitable gate decompositions for the MERA circuit, and the noise resilience of MERA, we achieve infidelities ranging from 10^{-4} to 10^{-2} . This enables the clear distinction between different entanglement scaling laws, even when the absolute difference in S is as small as ~ 0.15 .

Recall that we determine $\hat{\rho}_B$ through tomography on only $\sim T$ renormalized sites at the edge of subsystem A 's causal cone (cf. Sec. II), where, in the basis defined by \hat{U}_B , all other qubits are in the $|0\rangle$ state and need not be implemented. This is sufficient because the fidelity metric (3) and bipartite entanglement properties are invariant under the transformation \hat{U}_B , and it explains the high subsystem fidelities achieved in this work.

IV. OUTLOOK

We employed MERA on an ion-trap quantum computer to clearly resolve the quantum phase transition in a condensed matter system. The MERA allowed us to demonstrate the transition from area-law to log-area-law scaling in groundstate entanglement entropies. The experiment successfully captures the universal properties of Ising-class physics.

Extending this approach to other critical systems, including systems with higher spin and spatial dimensions, requires larger MERA bond dimensions χ . This, in turn, necessitates more qubits per renormalized site and more gates per MERA tensor [25–28]. Currently, MERA optimization relies on classical computation. However, as χ increases, the classical tensor contraction costs grow significantly, especially for higher-dimensional MERA (e.g., scaling between χ^{16} and χ^{26} for 2D systems [24, 59]). These costly classical contractions vanish when MERA is implemented on quantum computers, thereby achieving a polynomial quantum advantage [26, 27]. Additionally, mid-circuit qubit reset will reduce the total qubit count from $O(\log L)$ to $O(1)$ by reusing qubits in the MERA circuit that exit the causal cone [26, 60].

Recent advances in trapped-ion platforms have brought these capabilities closer to realization. For example, 56-qubit systems with 99.8% two-qubit gate fidelity are now available [61]. Larger systems, with ~ 200 qubits, can be achieved by scaling up the system used in this work [62]. The primary error source in high-connectivity ion systems—motional heating of low-frequency modes—can be reduced by over two orders of magnitude using cryogenic techniques and sympathetic cooling with a different isotopic species [63]. This approach also facilitates qubit reset and reuse, further enhancing scalability.

ACKNOWLEDGMENTS

T.W. thanks K. Sun and Y. Yu for valuable discussions.

Funding: This work was funded by the NSF Quantum Leap Challenge Institute for Robust Quantum Simulation (OMA-2120757) and the NSF STAQ project (Phy-2325080). Support is also acknowledged from the U.S. Department of Energy, Office of Science, National Quantum Information Science Research Centers, Quantum Systems Accelerator.

Author contributions: Q.M. designed the MERA implementation, conducted the numerical simulations, and analyzed the experimental data. T.W. executed the experiment and collected the experimental data. T.B. initiated the project and devised the holographic subsystem tomography. M.C. supervised the experimental work, while T.B. and K.R.B. supervised the theoretical effort. All authors contributed to the manuscript.

Competing interests: K.R.B. has a personal financial interest in the company IonQ. M.C. is a co-inventor on patents that are licensed by University of Maryland to IonQ, Inc. Other authors declare that they have no competing interests.

Appendix A: Trapped-ion system

Our experimental system consists of a linear chain of $^{171}\text{Yb}^+$ ions, spaced by approximately $3.7\ \mu\text{m}$, confined in a micro-fabricated Paul trap (Sandia HOA-2.1.1 [64]) held in a room-temperature vacuum chamber. The qubits are encoded in the hyperfine “clock” states of the ground $^2\text{S}_{1/2}$ electronic manifold as $|0\rangle \equiv |F = 0; m_F = 0\rangle$ and $|1\rangle \equiv |F = 1; m_F = 0\rangle$, where F is the total atomic angular momentum and m_F its projection on the magnetic field direction.

Qubits are initialized in the $|0\rangle$ state using optical pumping and measured by state-dependent fluorescence on the 369 nm D1 line. Qubits are manipulated via a Raman process using a wide ($300\ \mu\text{m} \times 30\ \mu\text{m}$) global-addressing beam and equispaced $1\ \mu\text{m}$ -diameter individual-addressing beams derived from the same 355-nm pulsed laser. Available single-qubit operations are virtual z -axis rotations $R_z(\theta)$, implemented via phase offsets in the radio-frequency controls, and physical xy -plane rotations $R(\theta, \phi) = e^{-i\theta(\hat{X}\cos\phi + \hat{Y}\sin\phi)/2}$. Entangling gates $XX(\theta) = e^{-i\theta\hat{X}_i \otimes \hat{X}_j/2}$ between arbitrary qubits i and j are realized through a Mølmer-Sørensen interaction mediated by the shared radial motional modes of the ion chain. This interaction is implemented by time-shaping the state-dependent force on the addressed ions using the 355-nm Raman process.

Appendix E describes experiments to characterize noise in the system and our corresponding error model.

Appendix B: Holographic subsystem tomography and entanglement scaling

For the study of bipartite entanglement entropies, entanglement spectra, and subsystem state fidelities as discussed in Sec. III, we consider MERA approximations $|\Psi\rangle$ for the ground state and a spatial bipartition into subsystem A and its complement B .

The goal of the holographic subsystem tomography is to efficiently access the reduced density matrix $\hat{\rho}_B = \text{Tr}_A |\Psi\rangle\langle\Psi|$ of subsystem B in the experiment. The isometric property ($W^\dagger \hat{W} = \mathbb{1}$) of the MERA tensors implies that, under the partial trace Tr_A , all tensors outside the causal cone of B can be removed, as exemplified by the shaded area atop subsystem A in Fig. 5. Furthermore, the aforementioned quantities are all invariant under unitary transformations on subsystem B . Using this invariance, we can remove all MERA gates outside the causal cone of subsystem A , which corresponds to

the action of the unitary transformation \hat{U}_B^\dagger from Sec. II. Only the gates inside the causal cone(s) of the subsystem boundary(ies) remain. All qubits outside this causal cone are in the reference state $|0\rangle$ and need not be implemented in the experiment.

To determine the transformed subsystem density matrix

$$\hat{U}_B^\dagger \hat{\varrho}_B \hat{U}_B = \text{Tr}_A(\hat{U}_B^\dagger |\Psi\rangle\langle\Psi| \hat{U}_B), \quad (\text{B1})$$

we only need to measure the $\sim T$ non-trivial renormalized sites at the edge of A 's causal cone, as indicated by the diamonds in Fig. 5. Again T denotes the number of MERA layers.

To further reduce experimental resource requirements, we consider either infinite chains with a bipartition into two semi-infinite subsystems, or finite chains with periodic boundary conditions where block B is large enough such that the causal cones of its two boundaries are disjoint as exemplified in Fig. 5. In the latter scenario, the transformed density operator (B1) is actually a tensor product of a state $\tilde{\varrho}_B^L$ at the left edge, a state $\tilde{\varrho}_B^R$ at the right edge, and central sites in the reference state $|0\rangle\langle 0|$,

$$\hat{U}_B^\dagger \hat{\varrho}_B \hat{U}_B = \tilde{\varrho}_B^L \otimes |0\rangle\langle 0| \otimes \dots \otimes |0\rangle\langle 0| \otimes \tilde{\varrho}_B^R. \quad (\text{B2})$$

Due to the product structure, $\tilde{\varrho}_B^L$ and $\tilde{\varrho}_B^R$ can be measured independently.

Moreover, when studying quantities that only depend on the spectrum of $\hat{\varrho}_B$ for a bipartition of the system into two equally sized halves and for total system sizes $L = 6 \times 2^T, 8 \times 2^T, \dots$, it is sufficient to measure only one of the two density operators. In this case, the MERA circuits for $\tilde{\varrho}_B^L$ and $\tilde{\varrho}_B^R$ prepare the same pure state, and only differ in the selection of sites to be measured: those at the right edge of the causal cone for $\tilde{\varrho}_B^L$ and those at the left edge for $\tilde{\varrho}_B^R$, as indicated in Fig. 5. Thus, all nonzero eigenvalues of $\hat{\varrho}_B$ are given by the elementwise product

$$\{\lambda_i \lambda_j\} \quad \text{of } \tilde{\varrho}_B^L \text{'s spectrum} \quad \{\lambda_i\} \quad (\text{B3})$$

with itself.

Appendix C: Subsystem size versus number of MERA layers

In the main text, we associated the number T of layers in infinite MERA with the logarithm of subsystem sizes ℓ . Here, we elaborate further on this relation.

Infinite binary 1D MERA $|\Psi\rangle$ with T layers have a maximum correlation range $\xi_{\max} := 3 \times 2^T$, where the prefactor 3 arises from the maximal causal-cone width of local operators acting on $k \leq 3$ contiguous sites. In particular, connected correlation functions

$$\langle \hat{O}_i \hat{O}'_{i+\delta\ell} \rangle_\Psi - \langle \hat{O}_i \rangle_\Psi \langle \hat{O}'_{i+\delta\ell} \rangle_\Psi \quad (\text{C1})$$

are exactly zero for all i and local operators \hat{O}_i and \hat{O}'_j whenever $\delta\ell \geq \xi_{\max} - 3 + k$.

Hence, all local observables, two-point correlation functions, and subsystem density matrices for blocks of $\ell \leq \xi_{\max}$ sites of an infinite MERA coincide with those of a corresponding finite-size MERA for a system of $2\xi_{\max} = 6 \times 2^T$ sites with periodic boundary conditions.

Furthermore, the half-chain density operator of an infinite T -layer MERA, considered in Sec. III, is given by

$$\hat{U}_B^\dagger \hat{\varrho}_B \hat{U}_B = \tilde{\varrho}_B^L \otimes |0\rangle\langle 0| \otimes |0\rangle\langle 0| \otimes \dots, \quad (\text{C2})$$

where $\tilde{\varrho}_B^L$ is the same state as the one in Eq. (B2) for an $\ell = 3 \times 2^T$ -site block in a periodic 6×2^T -site system, establishing the exponential relation between ℓ and T . The spectra of the states (C2) and (B2) are related by the elementwise product (B3).

Appendix D: Scale-invariant MERA

Scale-invariant MERA are designed for critical systems, where correlation lengths diverge. As shown in Fig. 6(a), they feature an elementary cell of tensors that repeats in the spatial and renormalization directions, in accordance with the self-similarity of critical systems.

Viewed in the renormalization direction, the scale-invariant MERA maps the local Hamiltonian of a critical system into an RG fixed point. Seen in reverse, the scale-invariant MERA acts as a quantum channel that iteratively refines the state, starting from an initial reference state and adding layers to construct the ground state of the critical system.

Consider spin sites 0 and 1. Their causal-cone state as indicated by the unshaded region in Fig. 6(a) is constructed by applying the same layer-transition channel \mathcal{M} (Fig. 6(b)) multiple times, where renormalized sites that leave the causal cone are traced out. \mathcal{M} is a quantum channel and can be diagonalized in bi-orthonormal operator bases such that

$$\mathcal{M}(\cdot) = |\hat{\varrho}_{\text{steady}}\rangle\langle\mathbb{1}| + \sum_{i>0} m_i |\hat{r}_i\rangle\langle\hat{\ell}_i|, \quad (\text{D1})$$

where $|m_i| < 1$ for all $i > 0$, and we use a super-bra-ket notation for the operator-basis elements according to the Hilbert-Schmidt inner product $\langle\langle \hat{L} | \hat{R} \rangle\rangle := \text{Tr}(\hat{L}^\dagger \hat{R})$. We initialize the MERA in the product state $|\mathbf{0}\rangle = |0, \dots, 0\rangle$ at the topmost (infinite) layer. The expectation value of a local observable $\hat{O}_{0,1}$ with the scale-invariant MERA then is

$$\lim_{T \rightarrow \infty} \text{Tr}(\hat{O}_{0,1} \mathcal{M}^T(|\mathbf{0}\rangle\langle\mathbf{0}|)) = \text{Tr}(\hat{O}_{0,1} \hat{\varrho}_{\text{steady}}). \quad (\text{D2})$$

See Fig. 6(d). Experimentally, we cannot directly implement MERA with an infinite number of layers. Instead, we truncate after layer T and use the top layer to prepare a two-site state $\hat{\varrho}'$ that maximizes the contribution of the dominant eigenmode $\hat{\varrho}_{\text{steady}}$ of the layer-transition channel (D1). This is achieved by choosing the gate angles

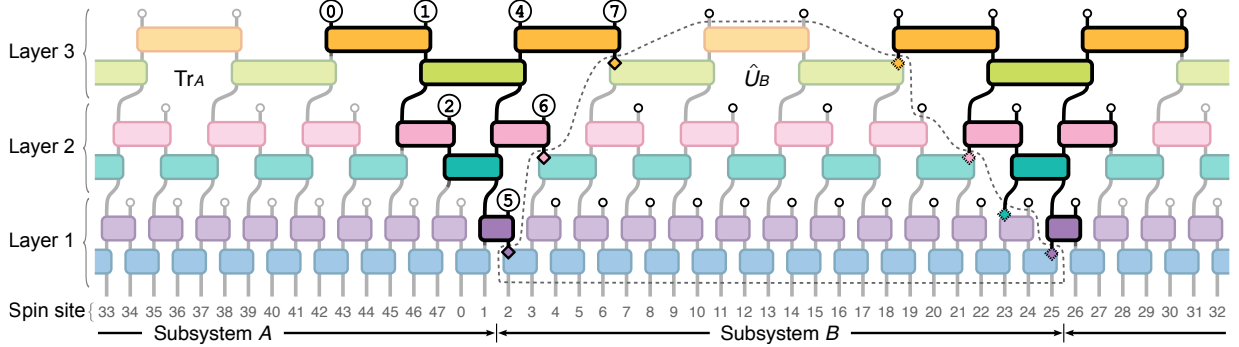


FIG. 5. Holographic subsystem tomography and entanglement scaling. An infinite binary MERA with T layers is consistent with a MERA on 6×2^T sites with periodic boundary conditions. Here, $T = 3$, resulting in a total of $6 \times 2^3 = 48$ sites. All connected two-point correlation functions for sites of distance $\geq 3 \times 2^T - 2 = 22$ are exactly zero. For example, $\langle \hat{X}_{10} \hat{Y}_{31} \rangle - \langle \hat{X}_{10} \rangle \langle \hat{Y}_{31} \rangle$ can be nonzero while $\langle \hat{X}_{10} \hat{Y}_{32} \rangle - \langle \hat{X}_{10} \rangle \langle \hat{Y}_{32} \rangle \equiv 0$. This is due to the fact that, in the latter case, the causal cones of the two operators have no overlap. Similarly, for any bipartition of the system into equally sized blocks like $A = \{26, \dots, 47, 0, 1\}$ and $B = \{2, \dots, 25\}$, the causal cones of the two subsystem boundaries do not overlap. Hence, measurements of the renormalized sites at the two boundaries are independent of each other, i.e., follow a product distribution.

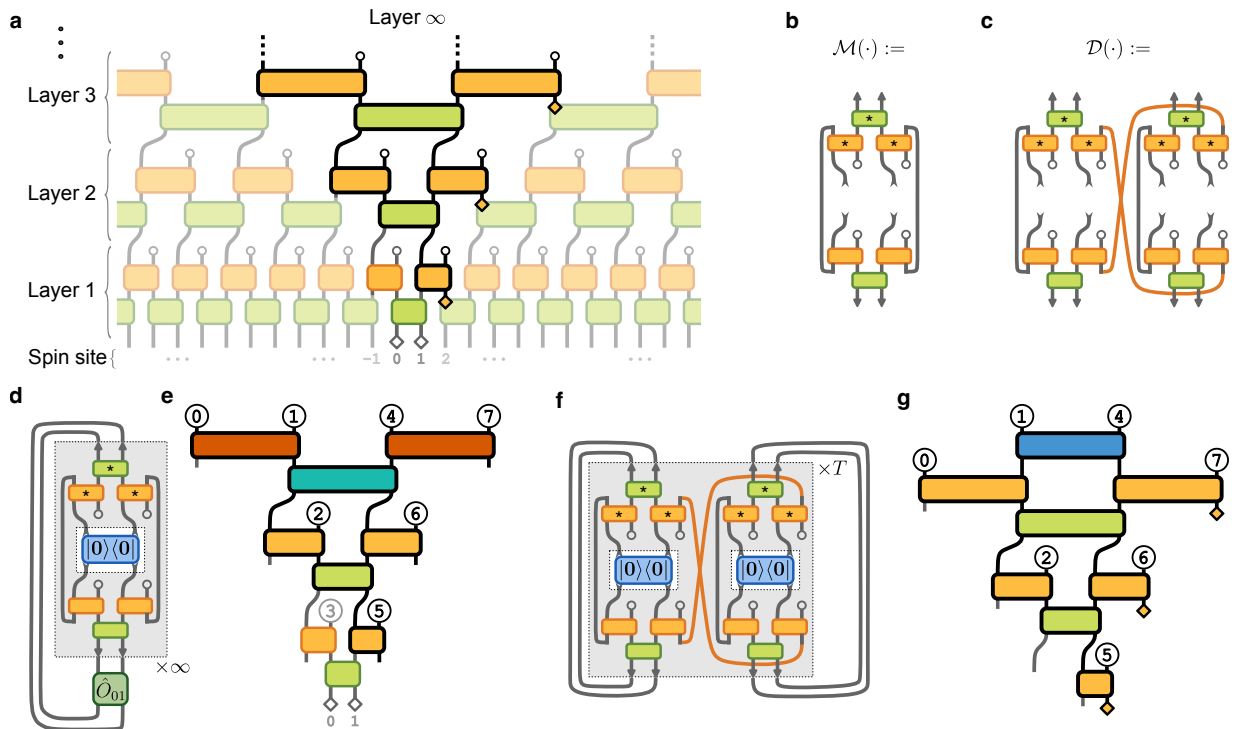


FIG. 6. Scale-invariant MERA and its implementation on the quantum computer. (a) A scale-invariant binary 1D MERA with an infinite number of lattice sites and layers. All unitaries (light-green boxes without open circles) and isometries (orange boxes with open circles) are identical across layers and the spatial direction. (b) Local observables on sites 0 and 1 have a causal cone consisting of a repeating configuration of tensors in each layer. The corresponding repeated layer-transition channel $\mathcal{M}(\cdot)$ maps reduced density matrices from the top to the bottom layer. Stars indicate complex conjugation. (c) The shown doubled and SWAP-contracted layer-transition map \mathcal{D} can be used to compute the second-order Rényi entanglement entropy of a bipartition into subsystems $(-\infty, 1]$ and $[2, \infty)$ (see panel f). (d) Causal-cone tensor-network for the evaluation of local expectation values on sites 0 and 1. The MERA circuit is initialized with reference state $|0\rangle$ at the top layer. (e) In the experiment, we truncate the scale-invariant MERA after layer T . For the measurement of local observables, the top layer is optimized to approximate the dominant eigenmode $\hat{\rho}_{\text{steady}} := \lim_{T \rightarrow \infty} \mathcal{M}^T(|0\rangle\langle 0|)$ of the layer-transition channel. Finally, we measure the qubits at sites 0 and 1. (f) The tensor network for the purity of the reduced density operator of subsystem $[2, \infty)$. (g) In this case, the top tensor (blue) is optimized to suppress sub-leading contributions from the eigenvectors of the doubled map \mathcal{D} . Scale-invariant layers are then appended. To extract the scaling of entanglement as a function of the number T of RG steps, we perform tomography on T qubits at the right edge of the boundary causal-cone circuit (see also Fig. 5).

$\{\theta\}$ in layer T as $\arg \min_{\theta} \sum_{i>0} |m_i \langle \hat{\ell}_i | \hat{\varrho}' \rangle|^2$. We then append $T - 1$ layers of the scale-invariant MERA to refine the dominant eigenmode as shown in Fig. 6(e). This approach is highly effective as demonstrated for $T = 5$ and a few local observables in Secs. III A and III B 1.

To account for layer truncations in the study of subsystem purity and entanglement, we introduce a doubled SWAP-contracted layer-transition map \mathcal{D} as shown in Fig. 6(c). For a scale-invariant MERA truncated after layer T and initialized with the reference state $|\mathbf{0}\rangle$, the purity of subsystem $B = [2, \infty)$ can be computed by iteratively applying \mathcal{D} to the (doubled) zero-product reference state $|\mathbf{0}, \mathbf{0}\rangle\langle\mathbf{0}, \mathbf{0}|$ at the topmost layer and taking the final trace as

$$\text{Tr}(\hat{\varrho}_B^2) = \text{Tr}(\mathcal{D}^T(|\mathbf{0}, \mathbf{0}\rangle\langle\mathbf{0}, \mathbf{0}|)); \quad (\text{D3})$$

see Fig. 6(f). Similarly to the channel \mathcal{M} , we can diagonalize \mathcal{D} such that $\mathcal{D}(\cdot) = \sum_i d_i |\hat{R}_i\rangle\langle\hat{L}_i|$ with $|d_0| > |d_i|$ for all $i > 1$. Due to the SWAP operation, \mathcal{D} is not a quantum channel and $|d_0| < 1$. The second-order Rényi entanglement entropy with $\alpha = 2$ in Eq. (2) evaluates to

$$\begin{aligned} S_B^{(2)} &= -\log_2 (\text{Tr}(\mathcal{D}^T(|\mathbf{0}, \mathbf{0}\rangle\langle\mathbf{0}, \mathbf{0}|))) \\ &= -\log_2 \left(\sum_{i=0} d_i^T \langle\langle \mathbb{1} | \hat{R}_i \rangle\langle \hat{L}_i | \mathbf{0}, \mathbf{0} \rangle \right) \\ &\rightarrow -T \log_2 d_0 - \log_2 \left(\langle\langle \mathbb{1} | \hat{R}_0 \rangle\langle \hat{L}_0 | \mathbf{0}, \mathbf{0} \rangle \right), \end{aligned} \quad (\text{D4})$$

where the large- T limit is taken in the last line, and $|\mathbf{0}, \mathbf{0}\rangle$ represents the projector $|\mathbf{0}, \mathbf{0}\rangle\langle\mathbf{0}, \mathbf{0}|$. Hence, the entanglement entropy should increase linearly with T , i.e., by a constant in each renormalization step.

Even with the small bond dimension $\chi = 2$, the dominant eigenvalue d_0 of \mathcal{D} in the optimized scale invariant MERA agrees well with the conformal field theory prediction for the Ising model with central charge $c = 1/2$:

$$-8 \log_2 d_0 = 0.475 \dots \approx c. \quad (\text{D5})$$

Again, we truncate the scale-invariant MERA after layer $T \leq 4$ for experiments. To mitigate the effect of the truncation, we do not initialize with the reference state $|\mathbf{0}\rangle$ at the top layer but with a more suitable two-site state $|\varphi\rangle$, generated from $|\mathbf{0}\rangle$ through one entangling and further single-qubit gates. These gates are chosen to suppress subleading contributions in (D4) by minimizing $\sum_{i>0} |d_i \langle\langle \mathbb{1} | \hat{R}_i \rangle\langle \hat{L}_i | \varphi, \varphi \rangle|^2$. Thus, we arrive at the approximation

$$S_B^{(2)} = -\log_2 (\text{Tr}(\mathcal{D}^T(|\varphi, \varphi\rangle\langle\varphi, \varphi|))) \approx -T \log_2 d_0. \quad (\text{D6})$$

After implementing such T -layer approximations of a scale-invariant MERA in the experiment, we perform the holographic subsystem tomography, measuring all T qubits at the right edge of the boundary causal-cone as discussed in Sec. B and illustrated in Fig. 6(g).

Appendix E: System characterization and error model

1. State preparation and measurement error

State preparation and measurement (SPAM) errors contribute significantly to our error budget. To quantify the probability p_d of SPAM errors for the dark state $(|0\rangle)$, we performed fluorescence detection after initializing all qubits via the usual optical pumping, yielding an average measured error of 0.16% (see Fig. 7 for detailed SPAM errors). To measure the probability p_b of SPAM errors for the bright state $(|1\rangle)$, we applied $R_y(\pi)$ gates following the optical pumping and then performed fluorescence detection, yielding an average measured error of 0.45% (see Fig. 7 for detailed SPAM errors). We checked the rotation error of the $R_y(\pi)$ gates by applying nine consecutive $R_y(\pi)$ -gates, yielding a population error of $0.56^{+0.17\%}_{-0.12\%}$ as determined by the binomial proportionate 95% confidence interval using the Clopper-Pearson method. The population error resulting from single-qubit gates should scale superlinearly with the number N of gates, corresponding to a mixture of uncorrelated and correlated noise. Our results imply a population error below 10^{-3} per π -gate, which is below the determined bright-state SPAM error.

The measurement error for the $^{171}\text{Yb}^+$ hyperfine qubits arises from optical pumping between the hyperfine states during the optical detection pulse [65, 66]. We fit the measured photon count statistics at various detection time τ to an optical pumping model as discussed below to determine the state preparation error and the measurement errors.

The distributions of detection counts for a single ion prepared in the bright state for different detection times are shown in Fig. 8(a). Ideally, the ion would cycle between the $|S, F = 1\rangle$ and $|P, F = 0\rangle$ manifolds, resulting in a Poisson distribution of the recorded photon counts. However, the bright state can be off-resonantly pumped to the dark hyperfine ground state via the $|S, F = 1\rangle \rightarrow |P, F = 1\rangle$ transition detuned by 2.1 GHz with a rate R_b that is about 5×10^4 times lower than the bright-state photon scattering rate Γ_{sc} . Neglecting the even slower dark-to-bright pumping process, the predicted distribution of the bright-state photon counts are

$$P_b(n) = e^{-R_b \tau} \mathcal{P}(n; \eta \Gamma_{\text{sc}} \tau) + \int_0^\tau e^{-R_b t} \mathcal{P}(n; \eta \Gamma_{\text{sc}} t) R_b dt, \quad (\text{E1})$$

where $\mathcal{P}(n; \bar{n}) = e^{-\bar{n}} \bar{n}^n / n!$ is the Poisson distribution with mean \bar{n} , and η is the detection efficiency. The red dashed curves in Fig. 8(a) show fits of the obtained count data to this model with $\eta \Gamma_{\text{sc}} \tau$ and R_b as the fitting parameters. We average the fitted R_b values with weights inversely proportional to the fitted variances to obtain $R_b = 3.0(1) \times 10^2 / \text{s}$. The detection count statistics for a single ion prepared in the dark $|S, F = 0\rangle$ state are shown in Fig. 8(b). The dark state can be off-resonantly

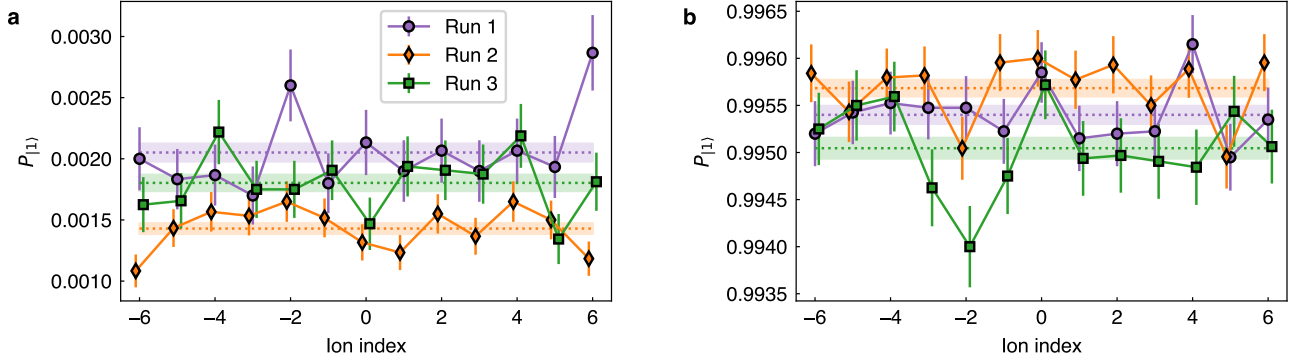


FIG. 7. State preparation and measurement (SPAM) population as a function of the ion index. (a) Dark-state ($|0\rangle$) SPAM experiments, with ion-averaged errors of 0.205(7)%, 0.143(4)%, and 0.180(7)% for three runs; (b) Bright-state ($|1\rangle$) SPAM experiments, with ion-averaged errors of 0.460(9)%, 0.432(9)%, and 0.495(11)% for three runs. Error bars and shaded areas indicate 1σ statistical intervals.

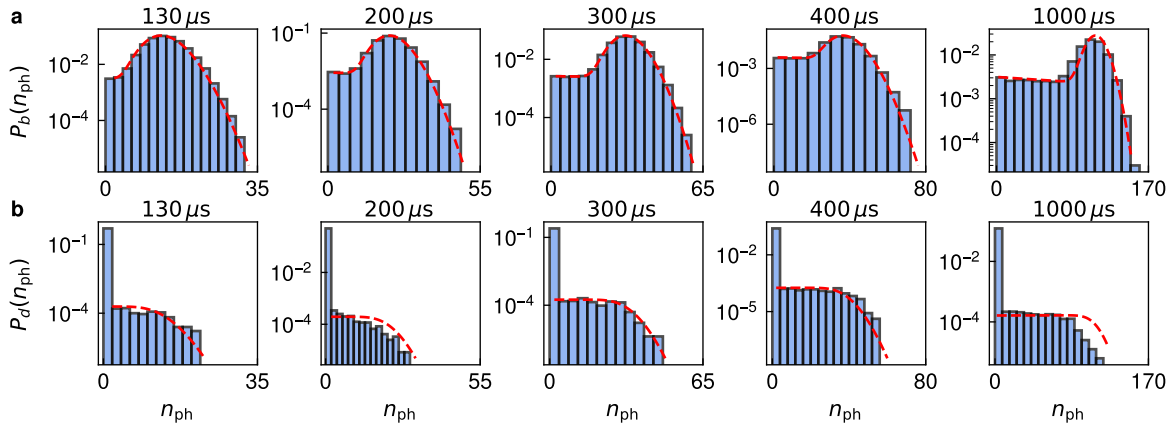


FIG. 8. Distribution of the detected photon counts n_{ph} for different detection times for the bright state (a) and the dark state (b). The red dashed lines indicate a fit to the models from Eq. (E1) and (E2).

pumped to the bright manifold via the 14.7-GHz detuned $|S, F = 0\rangle \rightarrow |P, F = 1\rangle$ transition, with a rate R_d that is about 10^6 times lower than Γ_{sc} . Neglecting the reverse pumping process yields the predicted dark-state count distribution

$$P_d(n) = \int_0^\tau \mathcal{P}(n; \eta \Gamma_{\text{sc}}(\tau - t)) e^{-R_d t} R_d \, dt. \quad (\text{E2})$$

Fitting this model to the count data for photon number $n_{\text{ph}} > 1$ in Fig. 8(b) yields $R_d = 18(1)/\text{s}$. The obtained ratio of R_b and R_d is close to the theoretical prediction in Ref. [67].

To distinguish the preparation error from the measurement error, we fitted the average dark-state photon number as a function of detection time τ (Fig. 9) to the rate equation model from Ref. [67]:

$$\bar{n}_{\text{ph}} = \int_0^\tau \eta \Gamma_{\text{sc}} \left(P_{d,\infty} - (p - P_{b,\infty}) e^{-(R_b + R_d)t} \right) dt, \quad (\text{E3})$$

where p is the state preparation error probability. Here, $P_{b,\infty} = (R_b/R_d + 1)^{-1}$ and $P_{d,\infty} = 1 - P_{b,\infty}$ are the

equilibrium bright and dark-state populations, respectively. The fitted value $p = 10(6) \times 10^{-5}$ confirms that our SPAM error is dominated by the measurement errors, as $p \ll p_d, p_b$.

To model state-preparation error in the numerical simulations, we flip each qubit with probability p . To simulate the detection error, after applying the circuit and measuring in the computational basis $\{|0\rangle, |1\rangle\}$, we randomly flip $|0\rangle \rightarrow |1\rangle$ with probability $p_d - p$ and $|1\rangle \rightarrow |0\rangle$ with probability $p_b - p$.

2. Idling noise

We characterized the dephasing of idle qubits using a Ramsey pulse sequence. After applying $R_y(\frac{\pi}{2})$ gates to all 13 qubits, we simulated idling by turning off the individual-addressing Raman beams while keeping the global beam on with the same settings as during a gate sequence. After a variable idle time τ_{idle} , we completed the Ramsey sequence with $R_z(\phi)$ and $R_y(\frac{\pi}{2})$ gates and

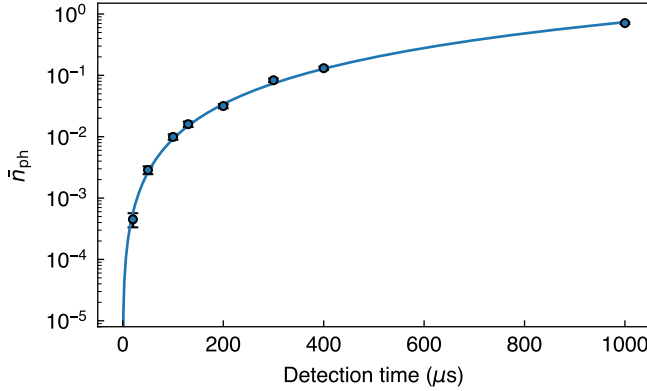


FIG. 9. The average number \bar{n}_{ph} of collected photons when preparing the ion in the $|0\rangle$ as a function of detection time τ . The error bars indicate 1σ confidence interval with 60,000 experimental shots.

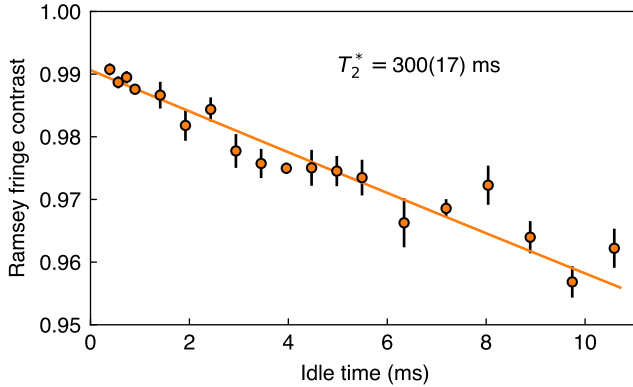


FIG. 10. The average qubit Ramsey fringe contrast as a function of the idle time τ_{idle} from a sample dataset. The orange line represents the fit to the model $A e^{-\tau_{\text{idle}}/T_2^*}$ yielding $T_2^* = 300(17) \text{ ms}$ and $A = 0.991(1)$. For the experimental data, error bars indicate 1σ fitting uncertainties.

recorded the $|1\rangle$ state population as a function of ϕ . We obtained the fitted ion-averaged contrast C from the resulting fringes and modeled it as $A e^{-\tau_{\text{idle}}/T_2^*}$. Fig. 10 shows a representative fit from a sample dataset, yielding $A = 0.991(1)$ and $T_2^* = 300(17) \text{ ms}$. The deviation of the fitted value of A from 1 mainly reflects SPAM errors, with additional contributions potentially arising from residual single-qubit gate errors and qubit addressing and detection crosstalk. From several datasets collected on different experimental days, the fitted T_2^* ranges from 260 ms to 370 ms, with an average of 290 ms. We attribute the measured dephasing to acoustic noise, mainly from air cooling fans, in our phase-sensitive Raman interferometer setup. We expect that T_2^* times of several seconds can be achieved using phase-insensitive schemes [68] that are compatible with our experimental setup.

In our simulations, we model the effects of dephasing on the qubit density matrix $\hat{\rho}$ over the time interval t via

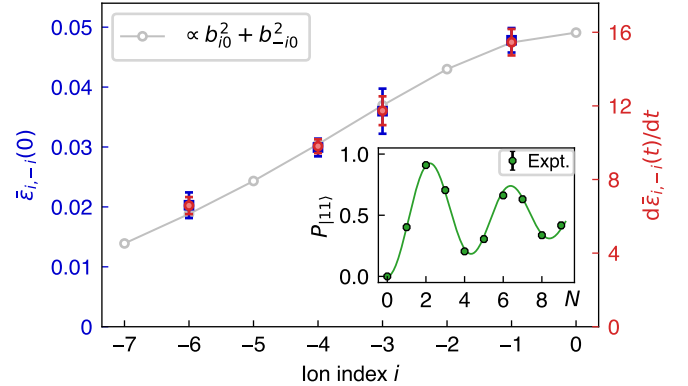


FIG. 11. The fitted initial decay parameter $\bar{\varepsilon}_{i,-i}(0)$ (blue) and its increase rate $d\bar{\varepsilon}_{i,-i}(t)/dt$ (red) for XX gates acting on ions i and $-i$. The gray line is proportional to the sum of squares $b_{i0}^2 + b_{-i0}^2$ of the participation factors for the addressed ions in the lowest axial mode of the ion chain. Error bars indicate 1σ fit uncertainties. The inset shows the $|1,1\rangle$ -state population for ions $(-3, 3)$ as a function of the gate number N after a wait time of $t \approx 10 \text{ ms}$, with a fit according to Eq. (E6).

the quantum channel

$$\mathcal{E}_Z(\hat{\rho}) = (1 - p_Z)\hat{\rho} + p_Z \hat{Z} \hat{\rho} \hat{Z}, \quad (\text{E4})$$

with the Z -flip probability $p_Z = t/(2T_2^*)$.

3. Gate errors

a. Axial motion

Axial motion of our 15-ion chain, dominated by the lowest-frequency axial mode (mode 0) with angular frequency $\omega_0 = 2\pi \times 241.8 \text{ kHz}$, is a leading error source in our platform. This motion misaligns the ions relative to the tightly-focused addressing beams, causing gate errors [63]. These errors increase over time as the ions' motion is driven by noisy electric fields.

We quantified the addressing error after a wait time t following laser cooling by applying a variable number N of $XX(\frac{\pi}{2})$ gates of total duration Δt to ions i and j and measuring the mean population $P_{|11\rangle}$ of the $|1,1\rangle$ state. The recorded populations $P_{|11\rangle}$ as a function of N for $(i, j) = (3, -3)$ are shown in the inset of Fig. 11. Uncertainty in the ions' axial motion translates into a variance in the total XX rotation angle, leading to damping of $P_{|11\rangle}$ oscillations.

The observed damping is governed by the statistics of the phonon number of mode 0 during gate application [63]. We model the evolution of the phonon number n_t at time t as a biased random walk. Since the energy of mode 0 following laser cooling corresponds to hundreds of phonons, and the average heating per XX gate corresponds to more than 20 phonons, we coarse-grain n_t on

intervals of size δn with $1 \leq \delta n \ll 2n_t$ and model the random walk as

$$n_{t+\delta t} := \begin{cases} n_t + \delta n & \text{with prob. } \frac{n_t + \delta n}{\delta n} \frac{\dot{n} \delta t}{\delta n} \\ n_t - \delta n & \text{with prob. } \frac{n_t - \delta n}{\delta n} \frac{\dot{n} \delta t}{\delta n} \\ n_t & \text{otherwise,} \end{cases} \quad (\text{E5})$$

where \dot{n} is the heating rate of mode 0, and the time step δt is chosen so that the change of $n_t/\delta n$ remains small ($\frac{2n_t + \delta n}{\delta n} \frac{\dot{n} \delta t}{\delta n} \leq 1$).

When initialized with a Boltzmann distribution with mean $\bar{n}_0 \gg 1$, n_t remains exponentially distributed with mean $\bar{n}_t = \bar{n}_0 + \dot{n}t$. In this thermal limit, the time-averaged phonon number $n_t^{\text{avg}} := \frac{1}{\Delta t} \int_t^{t+\Delta t} n_{t'} dt'$ between time t and $t + \Delta t$ has the mean $\mu_t = \bar{n}_{t+\Delta t/2} = \bar{n}_t + \dot{n} \frac{\Delta t}{2}$ and the variance $\sigma_t^2 = \mu_t^2 - \frac{\bar{n}_t \dot{n} \Delta t}{3} + \frac{\dot{n}^2 \Delta t^2}{6}$. The distribution of n_t^{avg} can be well approximated by a Gamma distribution with the corresponding mean and variance.

If N $XX(\theta)$ gates are applied between time t and $t + \Delta t$, neglecting other errors and assuming the above Gamma distribution, we obtain the population

$$P_{|11\rangle}(t) = \frac{1 - C \cos(N\theta - \phi)}{2}, \quad (\text{E6})$$

of the $|1,1\rangle$ state with phase shift $\phi = \alpha \arctan(\alpha N \theta \bar{\varepsilon}_{i,j}(t + \frac{\Delta t}{2}))$ and contrast $C = (1 + [\alpha N \theta \bar{\varepsilon}_{i,j}(t + \frac{\Delta t}{2})]^2)^{-\alpha/2}$, where $\alpha = \mu_t^2 / \sigma_t^2$ and $\bar{\varepsilon}_{i,j}(t) = \bar{\varepsilon}_i(t) + \bar{\varepsilon}_j(t)$. The mean dimensionless decay parameter $\bar{\varepsilon}_i(t)$ during the gate sequence is

$$\bar{\varepsilon}_i(t) = \frac{\hbar b_{i0}^2}{m \omega_0 w^2} \bar{n}_t, \quad (\text{E7})$$

where b_{i0} is the participation factor of ion i in mode 0. Here, we assume that the ion motion remains much smaller than our Gaussian-shaped beams. We determine the individual-beam waist w by fitting the dependence of the single-qubit Rabi frequency Ω on the axial ion position x to $\Omega_0 e^{-(x-x_0)^2/w^2}$, yielding $w = 646(12)$ nm. In the limit of negligible heating during the gate sequence, the prediction (E6) reduces to Eq. (4) in [63].

For different ion pairs $(i, j = -i)$, we fit the measured mean $|1,1\rangle$ -state population as a function of the gate number N and wait time t to the model (E6). The fitted dimensionless effective decay parameter $\bar{\varepsilon}_{i,j}(0)$ at $t = 0$ and its rate of increase $d\bar{\varepsilon}_{i,j}/dt$ are shown as functions of i in Fig. 11. Both parameters scale with $b_{i0}^2 + b_{j0}^2$, indicating that addressing errors are dominated by excitations of the lowest axial mode of the ion chain. The fitted initial phonon number in this mode is $\bar{n}_0 = 409(4)$ and the heating rate is $\dot{n} = 133(1)$ phonons/ms.

To model gate rotation errors for arbitrary single- and two-qubit gates, in each shot of the noisy simulations, we sample the initial phonon number n_0 from an exponential distribution with mean \bar{n}_0 . We then evolve n_t using the random walk model (E5). For

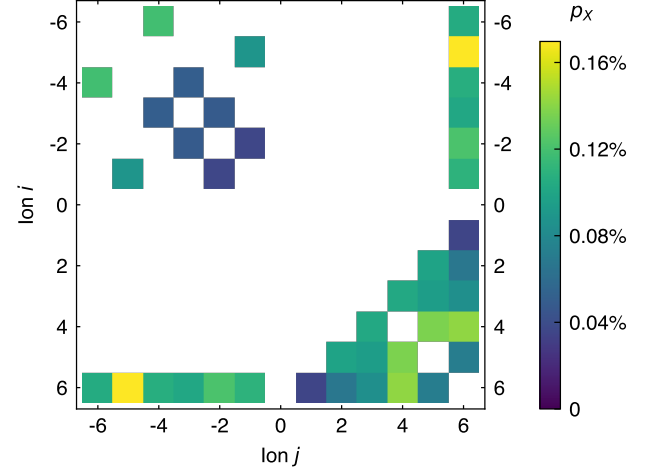


FIG. 12. Pauli X error $p_{X,i,j}(\pi/2)$ per fully-entangling XX gate acting on ions i and j ; cf. Eq. (E9). We only show error data for gate pairs that are actually utilized in this work.

each native gate in the circuit, we compute the time-averaged phonon number n_t^{avg} . In the noise model, the phonon number n_t^{avg} changes single-qubit gate rotations as $R(\theta) \rightarrow R(\theta(1 - n_t^{\text{avg}} \bar{\varepsilon}_i / \bar{n}_t))$ and two-qubit gate rotations as $XX(\theta) \rightarrow XX(\theta(1 - n_t^{\text{avg}} \bar{\varepsilon}_{i,j} / \bar{n}_t))$.

b. X -errors

We describe X -errors during an $XX(\theta)$ gate on ion pair (i, j) using a bit-flip channel acting on the density matrix $\hat{\rho}$ of ion i as

$$\mathcal{E}_X(\hat{\rho}) = (1 - p_X) \hat{\rho} + p_X \hat{X} \hat{\rho} \hat{X}, \quad (\text{E8})$$

where $p_X \equiv p_{X,i,j}(\theta)$ is the X -flip probability per gate.

X -errors can be caused by residual spin-motion entanglement at the end of Mølmer-Sørensen gates. They can be minimized by carefully choosing the motional detuning, gate duration, and envelope of the amplitude-modulated gate waveforms [69]. In-between experiment runs, we stabilized frequencies of the radial ion-motion modes via blue-sideband Ramsey spectroscopy. Each of the central 11 qubits was used to query one of 11 radial modes that are addressed by the entangling gate waveforms. The obtained spectroscopical data was used to automatically adjust the quadratic and quartic terms in the static axial potential of the trap and a common motional offset frequency for all gates.

After applying N consecutive $XX(\frac{\pi}{2})$ gates to the $|0,0\rangle$ state on ions i and j , we measured the probability of X -flip errors by tracking the population $P_{i,j}(N)$ of the $|0,1\rangle$ and $|1,0\rangle$ states (parity leakage). We distinguished X -flip errors from coherent XX gate crosstalk by focusing on the shots where only the target qubits are flipped. In the

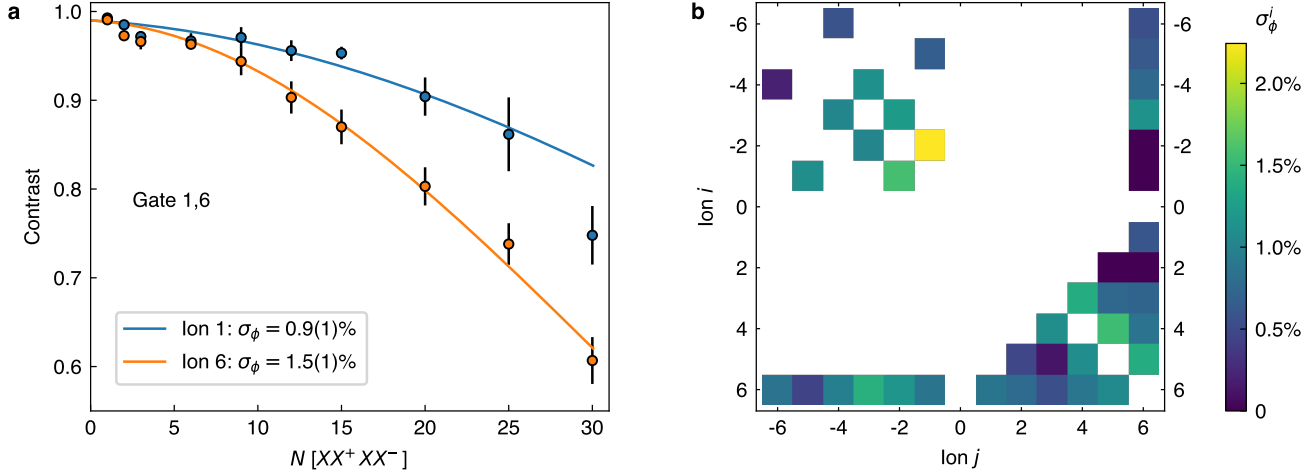


FIG. 13. (a) Ramsey fringe contrast as a function of the number of (XX^+, XX^-) gate pairs inside the Ramsey sequence for a sample gate. Solid lines indicate fits to a Gaussian function with zero mean and standard deviation $N\sigma_\phi^i$. (b) Standard deviation σ_ϕ^i of the random Gaussian-distributed phase shift ϕ_i on ion i per fully-entangling XX gate acting on ion pair (i, j) . Error data are shown only for gate pairs utilized in this work.

noise model (E8), we employ the X -flip error probability

$$p_{X,i,j}(\theta) = \frac{|\theta|}{\pi/2} \frac{P_{i,j}(N)}{2N}. \quad (\text{E9})$$

c. Z -errors

To measure Stark shifts during a specific XX gate, we insert N pairs of $XX(\frac{\pi}{2}) - XX(-\frac{\pi}{2})$ gates into a Ramsey pulse sequence consisting of initial $R_y(\frac{\pi}{2})$ and final $R_z(\phi) - R_y(\frac{\pi}{2})$ pulses applied to each targeted ion. After adjusting the qubit frequencies during the gate to compensate for the measured shifts, we use the same sequence to estimate any residual gate Z -errors.

The fitted contrast of the obtained Ramsey fringes for a sample gate is shown in Fig. 13(a). The observed dependence of the contrast on N is roughly quadratic, indicating that the phase shift error accumulates coherently as the number of gates increases. We model the observed decoherence by correlated fluctuations in the gate-induced

Stark shift, which can arise from fluctuations in the amplitude balance of the red and blue tones of the Mølmer-Sørensen gate due to air turbulence in the Raman beam setup. Since our Ramsey sequence prepares the qubits in the X -basis, we do not expect gate X -errors to affect the measured contrast. We assume that the phase shift ϕ_i induced on ion i by a fully-entangling XX gate during each shot follows a Gaussian distribution with zero mean and standard deviation σ_ϕ^i . This noise model results in a fringe contrast proportional to $e^{-(N\sigma_\phi^i)^2/2}$ to first order. Figure 13 show fits of this model to the measured contrast data and the fitted values of σ_ϕ^i for all fully-entangling XX gates on the ion pairs used in this work.

In the noise-model simulations, for each shot, we sample random numbers s from the Gaussian distribution $\mathcal{N}(0, 1)$. When executing quantum circuits, we replace the ideal $XX(\theta)$ gate by

$$e^{-\frac{i}{2}(\theta \hat{X}_i \hat{X}_j + \phi_i \hat{Z}_i + \phi_j \hat{Z}_j)}, \quad \text{where } \phi_i = s \frac{\sigma_\phi^i |\theta|}{\pi/2} \quad (\text{E10})$$

is a rescaled phase shift on ion i .

[1] S. L. Sondhi, S. M. Girvin, J. P. Carini, and D. Shahar, Continuous quantum phase transitions, *Rev. Mod. Phys.* **69**, 315 (1997).

[2] S. Sachdev, *Quantum Phase Transitions*, 2nd ed. (Cambridge University Press, Cambridge, UK, 2011).

[3] I. Bloch, J. Dalibard, and W. Zwerger, Many-body physics with ultracold gases, *Rev. Mod. Phys.* **80**, 885 (2008).

[4] A. Smith, M. Kim, F. Pollmann, and J. Knolle, Simulating quantum many-body dynamics on a current digital quantum computer, *npj Quantum Information* **5**, 106 (2019).

[5] F. Barratt, J. Dborin, M. Bal, V. Stojevic, F. Pollmann, and A. G. Green, Parallel quantum simulation of large systems on small nisq computers, *npj Quantum Information* **7**, 79 (2021).

[6] M. Meth, V. Kuzmin, R. van Bijnen, L. Postler, R. Stricker, R. Blatt, M. Ringbauer, T. Monz, P. Silvi, and P. Schindler, Probing phases of quantum matter with an ion-trap tensor-network quantum eigensolver, *Phys. Rev. X* **12**, 041035 (2022).

[7] J. Dborin, V. Wimalaweera, F. Barratt, E. Ostby, T. E.

O'Brien, and A. G. Green, Simulating groundstate and dynamical quantum phase transitions on a superconducting quantum computer, *Nature Communications* **13**, 5977 (2022).

[8] Q. Zhu, Z.-H. Sun, M. Gong, F. Chen, Y.-R. Zhang, Y. Wu, Y. Ye, C. Zha, S. Li, S. Guo, H. Qian, H.-L. Huang, J. Yu, H. Deng, H. Rong, J. Lin, Y. Xu, L. Sun, C. Guo, N. Li, F. Liang, C.-Z. Peng, H. Fan, X. Zhu, and J.-W. Pan, Observation of thermalization and information scrambling in a superconducting quantum processor, *Phys. Rev. Lett.* **128**, 160502 (2022).

[9] M. Tajik, M. Gluza, N. Sebe, P. Schüttelkopf, F. Cataldini, J. Sabino, F. Møller, S.-C. Ji, S. Erne, G. Guarneri, S. Sotiriadis, J. Eisert, and J. Schmiedmayer, Experimental observation of curved light-cones in a quantum field simulator, *Proceedings of the National Academy of Sciences* **120**, e2301287120 (2023).

[10] F. Fang, K. Wang, V. S. Liu, Y. Wang, R. Cimmino, J. Wei, M. Bintz, A. Parr, J. Kemp, K.-K. Ni, and N. Y. Yao, Probing critical phenomena in open quantum systems using atom arrays (2024), arXiv:2402.15376 [quant-ph].

[11] R. Islam, R. Ma, P. M. Preiss, M. Eric Tai, A. Lukin, M. Rispoli, and M. Greiner, Measuring entanglement entropy in a quantum many-body system, *Nature* **528**, 77 (2015).

[12] K. Li, M. Han, D. Qu, Z. Huang, G. Long, Y. Wan, D. Lu, B. Zeng, and R. Laflamme, Measuring holographic entanglement entropy on a quantum simulator, *npj Quantum Information* **5**, 30 (2019).

[13] A. Bergschneider, V. M. Klinkhamer, J. H. Becher, R. Klemt, L. Palm, G. Zürn, S. Jochim, and P. M. Preiss, Experimental characterization of two-particle entanglement through position and momentum correlations, *Nature Physics* **15**, 640 (2019).

[14] T. Brydges, A. Elben, P. Jurcevic, B. Vermersch, C. Maier, B. P. Lanyon, P. Zoller, R. Blatt, and C. F. Roos, Probing rényi entanglement entropy via randomized measurements, *Science* **364**, 260 (2019).

[15] M. Foss-Feig, S. Ragole, A. Potter, J. Dreiling, C. Figgatt, J. Gaebler, A. Hall, S. Moses, J. Pino, B. Spaun, B. Neyenhuis, and D. Hayes, Entanglement from tensor networks on a trapped-ion quantum computer, *Phys. Rev. Lett.* **128**, 150504 (2022).

[16] M. Tajik, I. Kukuljan, S. Sotiriadis, B. Rauer, T. Schweigler, F. Cataldini, J. Sabino, F. Møller, P. Schüttelkopf, S.-C. Ji, *et al.*, Verification of the area law of mutual information in a quantum field simulator, *Nature Physics* **19**, 1022 (2023).

[17] M. K. Joshi, C. Kokail, R. van Bijnen, F. Kranzl, T. V. Zache, R. Blatt, C. F. Roos, and P. Zoller, Exploring large-scale entanglement in quantum simulation, *Nature* **624**, 539 (2023).

[18] A. H. Karamlou, I. T. Rosen, S. E. Muschinske, C. N. Barrett, A. Di Paolo, L. Ding, P. M. Harrington, M. Hays, R. Das, D. K. Kim, *et al.*, Probing entanglement in a 2d hard-core bose–hubbard lattice, *Nature* **629**, 561 (2024).

[19] T. Barthel and J. Lu, Fundamental limitations for measurements in quantum many-body systems, *Phys. Rev. Lett.* **121**, 080406 (2018).

[20] J. R. McClean, S. Boixo, V. N. Smelyanskiy, R. Babbush, and H. Neven, Barren plateaus in quantum neural network training landscapes, *Nature Communications* **9**, 4812 (2018).

[21] M. Cerezo, A. Sone, T. Volkoff, L. Cincio, and P. J. Coles, Cost function dependent barren plateaus in shallow parametrized quantum circuits, *Nature Communications* **12**, 1791 (2021).

[22] G. Vidal, Entanglement renormalization, *Phys. Rev. Lett.* **99**, 220405 (2007).

[23] G. Vidal, Class of quantum many-body states that can be efficiently simulated, *Phys. Rev. Lett.* **101**, 110501 (2008).

[24] G. Evenbly and G. Vidal, Algorithms for entanglement renormalization, *Phys. Rev. B* **79**, 144108 (2009).

[25] R. Haghshenas, J. Gray, A. C. Potter, and G. K.-L. Chan, Variational power of quantum circuit tensor networks, *Phys. Rev. X* **12**, 011047 (2022).

[26] Q. Miao and T. Barthel, Quantum-classical eigensolver using multiscale entanglement renormalization, *Phys. Rev. Res.* **5**, 033141 (2023).

[27] Q. Miao and T. Barthel, Convergence and Quantum Advantage of Trotterized MERA for Strongly-Correlated Systems, *Quantum* **9**, 1631 (2025).

[28] R. Haghshenas, E. Chertkov, M. DeCross, T. M. Gatterman, J. A. Gerber, K. Gilmore, D. Gresh, N. Hewitt, C. V. Horst, M. Matheny, T. Mengle, B. Neyenhuis, D. Hayes, and M. Foss-Feig, Probing critical states of matter on a digital quantum computer, *Phys. Rev. Lett.* **133**, 266502 (2024).

[29] I. H. Kim and B. Swingle, Robust entanglement renormalization on a noisy quantum computer, arXiv:1711.07500 (2017).

[30] T. Barthel and Q. Miao, Absence of barren plateaus and scaling of gradients in the energy optimization of isometric tensor network states, arXiv:2304.00161, accepted in *Commun. Math. Phys.* (2025).

[31] Q. Miao and T. Barthel, Isometric tensor network optimization for extensive hamiltonians is free of barren plateaus, *Phys. Rev. A* **109**, L050402 (2024).

[32] J. Eisert, M. Cramer, and M. B. Plenio, Colloquium: Area laws for the entanglement entropy, *Rev. Mod. Phys.* **82**, 277 (2010).

[33] J. I. Latorre and A. Riera, A short review on entanglement in quantum spin systems, *J. Phys. A: Math. Theor.* **42**, 504002 (2009).

[34] N. Laflorencie, Quantum entanglement in condensed matter systems, *Phys. Rep.* **646**, 1 (2016).

[35] S. Montangero, M. Rizzi, V. Giovannetti, and R. Fazio, Critical exponents with a multiscale entanglement renormalization ansatz channel, *Phys. Rev. B* **80**, 113103 (2009).

[36] R. N. C. Pfeifer, G. Evenbly, and G. Vidal, Entanglement renormalization, scale invariance, and quantum criticality, *Phys. Rev. A* **79**, 040301 (2009).

[37] B. M. McCoy, Spin correlation functions of the $x - y$ model, *Phys. Rev.* **173**, 531 (1968).

[38] P. Pfeuty, The one-dimensional ising model with a transverse field, *Annals of Physics* **57**, 79 (1970).

[39] T. J. Osborne and M. A. Nielsen, Entanglement in a simple quantum phase transition, *Phys. Rev. A* **66**, 032110 (2002).

[40] H. A. Kramers and G. H. Wannier, Statistics of the two-dimensional ferromagnet. part i, *Phys. Rev.* **60**, 252 (1941).

[41] G. De Chiara, L. Lepori, M. Lewenstein, and A. Sanpera, Entanglement spectrum, critical exponents, and or-

der parameters in quantum spin chains, *Phys. Rev. Lett.* **109**, 237208 (2012).

[42] A. Osterloh, L. Amico, G. Falci, and R. Fazio, Scaling of entanglement close to a quantum phase transition, *Nature* **416**, 608 (2002).

[43] O. F. Syljuåsen, Entanglement and spontaneous symmetry breaking in quantum spin models, *Phys. Rev. A* **68**, 060301 (2003).

[44] T. R. de Oliveira, G. Rigolin, M. C. de Oliveira, and E. Miranda, Symmetry-breaking effects upon bipartite and multipartite entanglement in the xy model, *Phys. Rev. A* **77**, 032325 (2008).

[45] M. Srednicki, Entropy and area, *Phys. Rev. Lett.* **71**, 666 (1993).

[46] C. Callan and F. Wilczek, On geometric entropy, *Phys. Lett. B* **333**, 55 (1994).

[47] C. Holzhey, F. Larsen, and F. Wilczek, Geometric and renormalized entropy in conformal field theory, *Nucl. Phys. B* **424**, 443 (1994).

[48] M. M. Wolf, Violation of the entropic area law for fermions, *Phys. Rev. Lett.* **96**, 010404 (2006).

[49] D. Gioev and I. Klich, Entanglement entropy of fermions in any dimension and the Widom conjecture, *Phys. Rev. Lett.* **96**, 100503 (2006).

[50] T. Barthel, M.-C. Chung, and U. Schollwöck, Entanglement scaling in critical two-dimensional fermionic and bosonic systems, *Phys. Rev. A* **74**, 022329 (2006).

[51] H.-Y. Huang, R. Kueng, and J. Preskill, Predicting many properties of a quantum system from very few measurements, *Nature Physics* **16**, 1050 (2020).

[52] P. Calabrese and J. Cardy, Entanglement entropy and conformal field theory, *Journal of Physics A: Mathematical and Theoretical* **42**, 504005 (2009).

[53] Z. Hradil, Quantum-state estimation, *Phys. Rev. A* **55**, R1561 (1997).

[54] J. Řeháček, Z. Hradil, and M. Ježek, Iterative algorithm for reconstruction of entangled states, *Phys. Rev. A* **63**, 040303 (2001).

[55] J. Fiurášek, Maximum-likelihood estimation of quantum measurement, *Phys. Rev. A* **64**, 024102 (2001).

[56] D. F. V. James, P. G. Kwiat, W. J. Munro, and A. G. White, Measurement of qubits, *Phys. Rev. A* **64**, 052312 (2001).

[57] H. Li and F. D. M. Haldane, Entanglement spectrum as a generalization of entanglement entropy: Identification of topological order in non-abelian fractional quantum hall effect states, *Phys. Rev. Lett.* **101**, 010504 (2008).

[58] C. Kokail, R. van Bijnen, A. Elben, B. Vermersch, and P. Zoller, Entanglement hamiltonian tomography in quantum simulation, *Nature Physics* **17**, 936 (2021).

[59] T. Barthel and Q. Miao, Scaling of contraction costs for entanglement renormalization algorithms including tensor trotterization and variational monte carlo, *Phys. Rev. B* **111**, 045104 (2025).

[60] M. DeCross, E. Chertkov, M. Kohagen, and M. Foss-Feig, Qubit-reuse compilation with mid-circuit measurement and reset, *Phys. Rev. X* **13**, 041057 (2023).

[61] M. DeCross, R. Haghshenas, M. Liu, E. Rinaldi, J. Gray, Y. Alexeev, C. H. Baldwin, J. P. Bartolotta, M. Bohn, E. Chertkov, J. Cline, J. Colina, D. DelVento, J. M. Dreiling, C. Foltz, J. P. Gaebler, T. M. Gatterman, C. N. Gilbreth, J. Giles, D. Gresh, A. Hall, A. Hankin, A. Hansen, N. Hewitt, I. Hoffman, C. Holliman, R. B. Hutson, T. Jacobs, J. Johansen, P. J. Lee, E. Lehman, D. Lucchetti, D. Lykov, I. S. Madjarov, B. Mathewson, K. Mayer, M. Mills, P. Niroula, J. M. Pino, C. Roman, M. Schecter, P. E. Siegfried, B. G. Tiemann, C. Volin, J. Walker, R. Shaydulin, M. Pistoia, S. A. Moses, D. Hayes, B. Neyenhuis, R. P. Stutz, and M. Foss-Feig, *The computational power of random quantum circuits in arbitrary geometries* (2024), arXiv:2406.02501 [quant-ph].

[62] X.-C. Wu, D. M. Debroy, Y. Ding, J. M. Baker, Y. Alexeev, K. R. Brown, and F. T. Chong, Tilt: Achieving higher fidelity on a trapped-ion linear-tape quantum computing architecture, in *2021 IEEE International Symposium on High-Performance Computer Architecture (HPCA)* (2021) pp. 153–166.

[63] M. Cetina, L. Egan, C. Noel, M. Goldman, D. Biswas, A. Risinger, D. Zhu, and C. Monroe, Control of transverse motion for quantum gates on individually addressed atomic qubits, *PRX Quantum* **3**, 010334 (2022).

[64] P. L. W. Maunz, High optical access trap 2.0., [osti.gov , SAND](https://www.osti.gov/sand) (2016).

[65] S. Crain, C. Cahall, G. Vrijen, E. E. Wollman, M. D. Shaw, V. B. Verma, S. W. Nam, and J. Kim, High-speed low-crosstalk detection of a 171yb+ qubit using superconducting nanowire single photon detectors, *Commun Phys* **2**, 1 (2019).

[66] C. Roman, A. Ransford, M. Ip, and W. C. Campbell, Coherent control for qubit state readout, *New J. Phys.* **22**, 073038 (2020).

[67] R. Noek, G. Vrijen, D. Gaultney, E. Mount, T. Kim, P. Maunz, and J. Kim, High speed, high fidelity detection of an atomic hyperfine qubit, *Opt. Lett., OL* **38**, 4735 (2013).

[68] J. M. Pino, J. M. Dreiling, C. Figgatt, J. P. Gaebler, S. A. Moses, M. Allman, C. Baldwin, M. Foss-Feig, D. Hayes, K. Mayer, *et al.*, Demonstration of the trapped-ion quantum ccd computer architecture, *Nature* **592**, 209 (2021).

[69] S. Huang, K. R. Brown, and M. Cetina, Comparing shor and steane error correction using the bacon-shor code, *Science Advances* **10**, eadp2008 (2024).